Article

High-fidelity laser-free universal control of trapped ion qubits

https://doi.org/10.1038/s41586-021-03809-4

Received: 1 April 2021

Accepted: 7 July 2021

Published online: 8 September 2021

Check for updates

R. Srinivas[1,2,8]✉, S. C. Burd[1,2,9], H. M. Knaack[1,2], R. T. Sutherland[3,4,5], A. Kwiatkowski[1,2], S. Glancy[1], E. Knill[1,6], D. J. Wineland[1,2,7], D. Leibfried[1], A. C. Wilson[1], D. T. C. Allcock[1,2,7] & D. H. Slichter[1]✉

Universal control of multiple qubits—the ability to entangle qubits and to perform arbitrary individual qubit operations[1]—is a fundamental resource for quantum computing[2], simulation[3] and networking[4]. Qubits realized in trapped atomic ions have shown the highest-fidelity two-qubit entangling operations[5–7] and single-qubit rotations[8] so far. Universal control of trapped ion qubits has been separately demonstrated using tightly focused laser beams[9–12] or by moving ions with respect to laser beams[13–15], but at lower fidelities. Laser-free entangling methods[16–20] may offer improved scalability by harnessing microwave technology developed for wireless communications, but so far their performance has lagged the best reported laser-based approaches. Here we demonstrate high-fidelity laser-free universal control of two trapped-ion qubits by creating both symmetric and antisymmetric maximally entangled states with fidelities of $1^{+0}_{-0.0017}$ and $0.9977^{+0.0010}_{-0.0013}$, respectively (68 per cent confidence level), corrected for initialization error. We use a scheme based on radiofrequency magnetic field gradients combined with microwave magnetic fields that is robust against multiple sources of decoherence and usable with essentially any trapped ion species. The scheme has the potential to perform simultaneous entangling operations on multiple pairs of ions in a large-scale trapped-ion quantum processor without increasing control signal power or complexity. Combining this technology with low-power laser light delivered via trap-integrated photonics[21,22] and trap-integrated photon detectors for qubit readout[23,24] provides an opportunity for scalable, high-fidelity, fully chip-integrated trapped-ion quantum computing.

In trapped-ion systems, the entangling interactions required for universal control typically rely on an effective qubit–qubit coupling mediated by the shared motion of the ions[25–29]. Realizing this coupling requires control fields at the ions' positions that have strong spatial gradients on the length scale of the ions' zero-point motion (usually a few nanometres), commonly generated using laser light with wavelengths of a few hundred nanometres. Laser light can also be tightly focused to illuminate specific ions, providing individual qubit control[30]. Laser-based universal control[9–12] and two-qubit entanglement generation[31,32] in trapped ion qubits have been demonstrated, with refs. [5–7] reporting fidelities for symmetric Bell states of 0.9989(7), 0.9992(4) and 0.9994(3) (68% confidence level), respectively, where the results in refs. [5,6] are corrected for errors not induced by the entangling operation. These results represent the current state of the art for any quantum system. The achievements in refs. [5–7,9–12] relied on specialized high-performance laser systems, and the record fidelities in refs. [5,6] were limited primarily by off-resonant photon scattering[33], whereas ref. [7] was limited by laser intensity and phase noise. Laser-free trapped-ion entangling operations, which eliminate these sources of error, have been proposed[16–18] and demonstrated using microwave-frequency[19,20,34,35] or static[36,37] magnetic field gradients. Individual laser-free addressing can be achieved using spatial gradients of magnetic or electric fields[36,38–40] instead of focused laser beams. However, the highest-fidelity laser-free entangling interactions so far[19,20] have approximately three to five times larger corrected Bell-state infidelities than the laser-based interactions in refs. [5–7] and are more than an order of magnitude slower.

Here we demonstrate a new laser-free entangling method using an oscillating near-field radiofrequency magnetic field gradient, achieving a symmetric Bell-state fidelity of $1^{+0}_{-0.0017}$, corrected for initialization error. This fidelity is statistically indistinguishable from the highest-fidelity laser-based demonstrations, and the entangling operation is about four times faster than the previous highest-fidelity laser-free demonstrations. Our scheme is intrinsically robust to decoherence of both the ions' qubit[41] and motional[42] states, and enables the individual qubit addressing required for universal control using the same radiofrequency control fields that perform the entangling

[1]National Institute of Standards and Technology, Boulder, CO, USA. [2]Department of Physics, University of Colorado, Boulder, CO, USA. [3]Physics Division, Physical and Life Sciences, Lawrence Livermore National Laboratory, Livermore, CA, USA. [4]Department of Electrical and Computer Engineering, University of Texas at San Antonio, San Antonio, TX, USA. [5]Department of Physics and Astronomy, University of Texas at San Antonio, San Antonio, TX, USA. [6]Center for Theory of Quantum Matter, University of Colorado, Boulder, CO, USA. [7]Department of Physics, University of Oregon, Eugene, OR, USA. [8]Present address: Department of Physics, Clarendon Laboratory, University of Oxford, Oxford, UK. [9]Present address: Department of Physics, Stanford University, Stanford, CA, USA. ✉e-mail: raghavendra.srinivas@colorado.edu; daniel.slichter@nist.gov

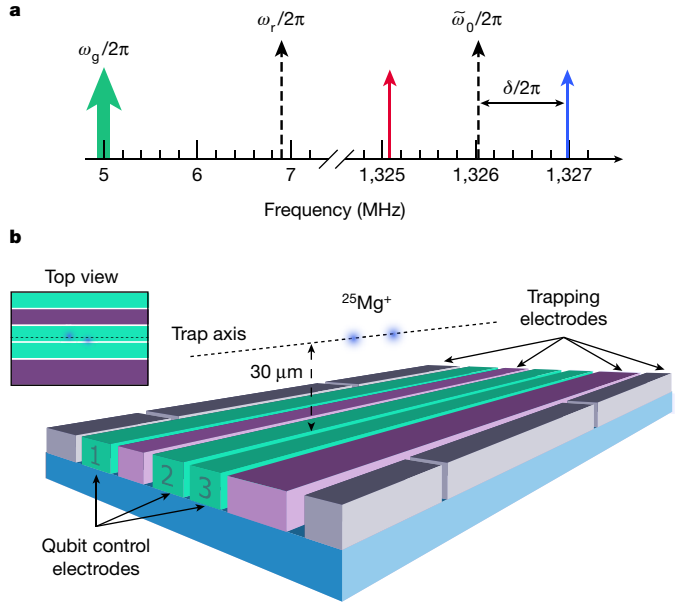

Fig. 1 | Experimental setup. a, Spectrum of applied currents. We apply currents with an approximately 1 A peak at $\omega_g = 2\pi \times 5$ MHz, close to the ions' motional frequency $\omega_r = 2\pi \times 6.9$ MHz, to create a magnetic field gradient at the ions (Supplementary Information). We also apply two much weaker currents (tens of milliamperes peak), symmetrically detuned by $\delta \approx (\omega_r - \omega_g)/2$ from the qubit frequency $\widetilde{\omega}_0 \approx 2\pi \times 1.326$ GHz, to generate the entangling interaction. We indicate the motional mode and qubit frequencies with dashed arrows. **b**, Three-dimensional perspective view of the central region of the surface-electrode ion trap (not to scale). For these experiments, we trap two $^{25}Mg^+$ ions approximately 30 μm above the trap surface. The megahertz and gigahertz currents used to generate the entangling interaction are driven along the qubit control electrodes (green, numbered 1–3) and create magnetic fields and field gradients transverse to the trap axis, whereas the confining potential is created by oscillating and static voltages applied to the purple and grey trapping electrodes, respectively. We adjust the orientation of the transverse modes (Supplementary Information) to maximize the magnetic field gradient along the mode at ω_r. We can apply static electric fields to rotate the ion crystal slightly with respect to the qubit control electrodes (inset), such that the two ions experience different a.c. Zeeman shifts from the magnetic field at ω_g. The same ion crystal configuration can be used both for entanglement and individually addressed control.

interaction. We use this universal control to create antisymmetric Bell states—which requires individual qubit control—with a fidelity of $0.9977^{+0.0010}_{-0.0013}$, corrected for initialization error, which is, to the best of our knowledge, the highest so far in any qubit platform.

The entangling operation relies on control signals at three frequencies, as shown in Fig. 1a. A strong magnetic field gradient with amplitude 152(15) T m^{-1} oscillating at frequency $\omega_g = 2\pi \times 5$ MHz, close to the frequency ω_r of one of the ions' out-of-phase radial (transverse to the trap axis) motional modes at $\omega_r \approx 2\pi \times 6.9$ MHz, is combined with two additional weaker microwave magnetic fields, symmetrically detuned by δ from the qubit frequency $\widetilde{\omega}_0 \approx 2\pi \times 1.326$ GHz, which is shifted from its nominal value of ω_0 by residual magnetic fields oscillating at ω_g. Previous laser-free entanglement demonstrations have required two high-power signals at gigahertz (rather than megahertz) frequencies to generate large gradients[19,20,34], or eight microwave fields (four per qubit) along with a strong static magnetic field gradient[37].

Choosing $\delta = (\omega_r - \omega_g)/2 + \Delta/2$, where $|\Delta| \ll |\omega_r - \omega_g|$ is a small frequency offset, the slowly rotating terms generate the interaction[41] (Supplementary Information)

$$\hat{H}_I(t) = \hbar\Omega_g J_2\left(\frac{4\Omega_\mu}{\delta}\right)(\hat{\sigma}_{z1} - \hat{\sigma}_{z2})(\hat{a}e^{i\Delta t} + \hat{a}^\dagger e^{-i\Delta t}), \quad (1)$$

which is used to implement a geometric phase gate[26–29], entangling the ion states via their shared motion with an effective $\hat{\sigma}_{z1}\hat{\sigma}_{z2}$ coupling. Here Ω_g and Ω_μ are proportional to the amplitude of the radiofrequency gradient and the microwave fields, respectively[41,43], J_n is the nth Bessel function of the first kind, the Pauli operator $\hat{\sigma}_{zi}$ acts on ion i, $\hat{a}(\hat{a}^\dagger)$ are the annihilation (creation) operators for the ions' selected motional mode, $\hbar$ is the reduced Planck's constant, and t is the interaction duration. By tuning the amplitude Ω_μ of the two microwave fields to an appropriate value (an 'intrinsic dynamical decoupling' or 'IDD' point), the qubits are dynamically decoupled from dephasing noise at frequencies well below δ, without requiring any additional control fields[41]. The microwave fields modulate the qubit state such that the effect of low-frequency dephasing noise on the qubit is multiplied by a prefactor of $J_0(4\Omega_\mu/\delta)$; the IDD points occur when Ω_μ is set such that $J_0(4\Omega_\mu/\delta) = 0$. We can also interleave the application of the interaction in equation (1) with a sequence of global qubit π pulses. These pulses suppress errors due to static or slowly varying (relative to $1/\Delta$) qubit frequency offsets, which are proportional to $\hat{\sigma}_{zi}$ and thus commute with the entangling interaction (see Supplementary Information). These same π pulses simultaneously implement Walsh modulation, which provides robustness to static offsets and slowly varying (relative to $1/\Delta$) drifts in the motional frequency or in the control field amplitudes (Supplementary Information)[42]. This combination of techniques yields an entangling interaction with substantial protection against decoherence of both the qubit and the ion motion, as well as experimental miscalibrations. Although our method can also generate an effective $\hat{\sigma}_{y1}\hat{\sigma}_{y2}$ interaction[41] with a different choice of δ, such an interaction would not commute with $\hat{\sigma}_{zi}$ errors and is therefore less desirable.

The experimental setup is similar to that in ref. [43], with radiofrequency and microwave control currents, as well as trapping voltages, applied to electroplated gold electrodes on a surface-electrode trap as shown in Fig. 1b. The trap is cooled to about 15 K, and we perform our operations on two $^{25}Mg^+$ ions held approximately 30 μm above the trap surface. We use the $|F = 3, m_F = 3\rangle \equiv |\downarrow\rangle$ and $|F = 2, m_F = 2\rangle \equiv |\uparrow\rangle$ states within the ions' $^2S_{1/2}$ ground-state hyperfine manifolds as our qubit states, where F is the total angular momentum and m_F is its projection along the quantization axis defined by a 21.3 mT static magnetic field. We present complete details of the experimental setup in the Supplementary Information.

Our scheme requires a magnetic-field-sensitive qubit transition, so the qubit coherence time is limited by magnetic field fluctuations. We investigate the performance of IDD, which should reduce the impacts of such fluctations, by observing the qubit coherence of a single ion in a spin-echo experiment without applying the oscillating gradient. We compare two cases: either no fields are applied during the spin-echo arms, or we apply two microwave fields, symmetrically detuned about the qubit frequency by δ, during both arms of the spin echo. The amplitudes of these fields are set to the IDD point $\Omega_\mu/\delta \approx 0.601$, where $J_0(4\Omega_\mu/\delta) = 0$ and the effects of low-frequency dephasing noise are thus suppressed[41]. Figure 2a shows that including IDD during the spin-echo arms increases the spin-echo coherence time by more than an order of magnitude. As the gradient at ω_g is not being applied, these microwave fields realize IDD but do not drive qubit-motion coupling.

Our entangling operation ideally transforms the initial state $|\downarrow\downarrow\rangle$ to the symmetric $|\Phi\rangle \equiv \frac{1}{\sqrt{2}}(|\downarrow\downarrow\rangle + i|\uparrow\uparrow\rangle)$ Bell state. We generate this entangling operation by applying the gradient and microwave fields as shown in Fig. 1a, using a sequence of eight pulses of simultaneously applied radiofrequency and microwave currents, interleaved with five qubit π pulses, and a π/2 pulse at the beginning and end of the sequence (Supplementary Fig. 2). This entire operation has a total duration of 740 μs (Supplementary Information). To achieve the highest fidelities, we sideband-cool[31] both the motional mode used for the entangling operation and the out-of-phase axial mode beforehand (Supplementary Information).

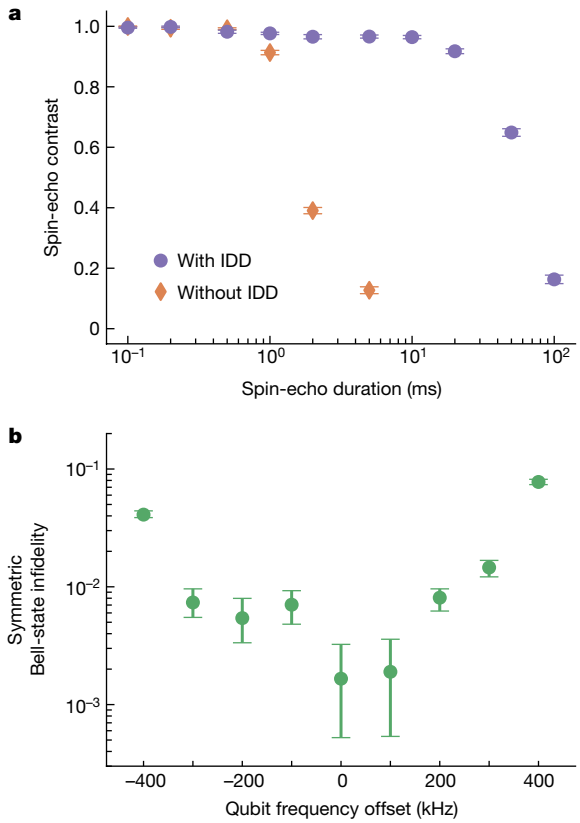

Fig. 2 | Robustness of entangling operation. a, Single-ion qubit coherence with and without IDD. We plot spin-echo contrast as a function of the total duration of both spin-echo arms. The data are shown either with (purple circles) or without (orange diamonds) application of microwave fields tuned to the IDD point during the spin-echo arms. **b**, Symmetric Bell-state infidelity versus qubit frequency offset. The qubit frequency is offset from the midpoint between the two microwave drive tones. For offsets of up to ±200 kHz, the symmetric Bell-state infidelity is still less than 10^{-2}, demonstrating the robustness of the entangling operation to such offsets, or to differences between the frequencies of the qubits. The data in **b** were taken separately from the highest-fidelity data reported in the main text, and the entangling operation fidelity was not fully optimized. Error bars in both panels indicate 68% confidence intervals.

The fidelity of the prepared state is determined by a parity analysis method[44] (Supplementary Information). We measure the probabilities P_0, P_1 and P_2 of finding 0, 1 or 2 ions in $|\downarrow\rangle$, respectively, either immediately after the entangling sequence, or after a subsequent π/2 analysis pulse with a variable phase. In the latter case, we determine the parity $P_0 + P_2 - P_1$ as a function of the analysis pulse phase as shown in Fig. 3a. We use these data to determine the Bell-state fidelity using maximum likelihood estimation.

To characterize the performance of the entangling operation, we seek to estimate the fidelity with which the operation could create a Bell state from a pure unentangled input state. As the experimental input states were not perfectly pure, we correct our reported Bell-state fidelities for initialization outside the $\{|\downarrow\rangle, |\uparrow\rangle\}$ manifold that occurs with probability $3.5(2) \times 10^{-3}$ per qubit (Supplementary Information). Owing to statistical uncertainty in both the raw fidelity estimate (which is constrained to be between 0 and 1) and the estimate of the state initialization error, it is possible to calculate a corrected fidelity greater than 1, in which case we truncate the estimate to the physical maximum of 1. We recorded multiple independent datasets while adjusting experimental parameters to optimize the fidelity. To avoid selection bias in choosing which dataset to report, we divided each dataset in half deterministically and used the extracted fidelity of one half as a 'trigger'. The fidelities reported here are determined by selecting the dataset with the highest 'trigger' fidelity and reporting the fidelity estimated only from the other half of that dataset. To characterize the uncertainty in the estimated fidelity, we performed bootstrapping of the data. Analysis details are presented in the Supplementary Information.

The estimated fidelity of the state produced (ideally $|\Phi\rangle$) for the dataset with the highest 'trigger' fidelity, corrected for the initialization error, was 1. From the distribution of bootstrapped fidelities, we determined a 68% confidence interval on the fidelity of [0.9983, 1] and a median bootstrap fidelity of 1. As an additional cross-check, we calculated the fidelity using an unbiased linear estimator instead of the maximum likelihood parity analysis, obtaining consistent results (Supplementary Information). In Fig. 3b, we compare the Bell-state fidelity and confidence interval to those of the highest-fidelity entangled states generated by laser-based[5–7] and laser-free[19,20] methods. We estimate that the leading sources of infidelity are decoherence of the ion motion such as motional dephasing, motional frequency drifts and motional heating, giving a total estimated infidelity of approximately 7×10^{-4}, on the basis of independent calibrations and numerical simulations (Supplementary Information). These errors are consistent with the experimental results given the uncertainty in the fidelity estimate. The motional errors could in principle be reduced further by increasing the interaction strength, performing a gate sequence with more phase-space loops or by using more complicated phase-space trajectories[45]. Future work will aim to reduce the uncertainty in the fidelity estimate and to characterize the entangling interaction using randomized benchmarking[46,47].

We also investigate the entangling operation's robustness to qubit frequency offsets ε that cause errors of the form $\frac{\hbar\varepsilon}{2}\hat{\sigma}_{zi}$, which commute with the interaction in equation (1). The π pulses in the gate sequence and the IDD should both provide protection against such errors. To characterize this effect, we intentionally add a common offset to the frequencies of the detuned microwave fields with respect to the qubit frequency, then perform the entangling interaction and measure the Bell-state fidelity, keeping all other parameters constant. As shown in Fig. 2b, the Bell-state infidelity remains below 10^{-2} for frequency offsets up to ±200 kHz.

This insensitivity to qubit frequency offsets enables individual addressing of the ions in frequency space without compromising entanglement fidelity. Individual addressing of trapped ion qubits has been demonstrated previously using tightly focused laser beams[9–12,30], and without lasers using static magnetic field gradients[36,39,48] and oscillating magnetic field gradients[40,49] at gigahertz frequencies. In our system, the currents at ω_g in the three-qubit control electrodes give rise to a magnetic field with a strong spatial gradient, but nearly zero field amplitude along the quantization axis, at the ion positions. The residual magnetic field at ω_g induces an a.c. Zeeman shift on the qubit transition frequency (Supplementary Information). We apply static electric fields to rotate the ion crystal slightly with respect to the trap axis (Fig. 1b, inset), such that the two ions experience different a.c. Zeeman shifts when the drive at ω_g is applied; we choose the ion positions to produce a differential shift of approximately 20 kHz (we use this same ion crystal configuration when performing entangling operations). The differential a.c. Zeeman shift generates differential phase evolution of the two qubits, enabling universal control when combined with global control pulses. For example, we can flip the spin of one of the two qubits using a spin-echo sequence of approximately 70 μs duration (Supplementary Information). With this individual control of our qubits, we transform the symmetric entangled state $|\Phi\rangle$ into an antisymmetric entangled state $|\Psi_-\rangle$:

$$|\Phi\rangle = \frac{1}{\sqrt{2}}(|\downarrow\downarrow\rangle + i|\uparrow\uparrow\rangle) \Rightarrow |\Psi_-\rangle = \frac{1}{\sqrt{2}}(|\downarrow\uparrow\rangle - |\uparrow\downarrow\rangle). \quad (2)$$

After creating the antisymmetric state $|\Psi_-\rangle$, we measure the ion populations and parity as before. As $|\Psi_-\rangle$ is invariant under global rotations,

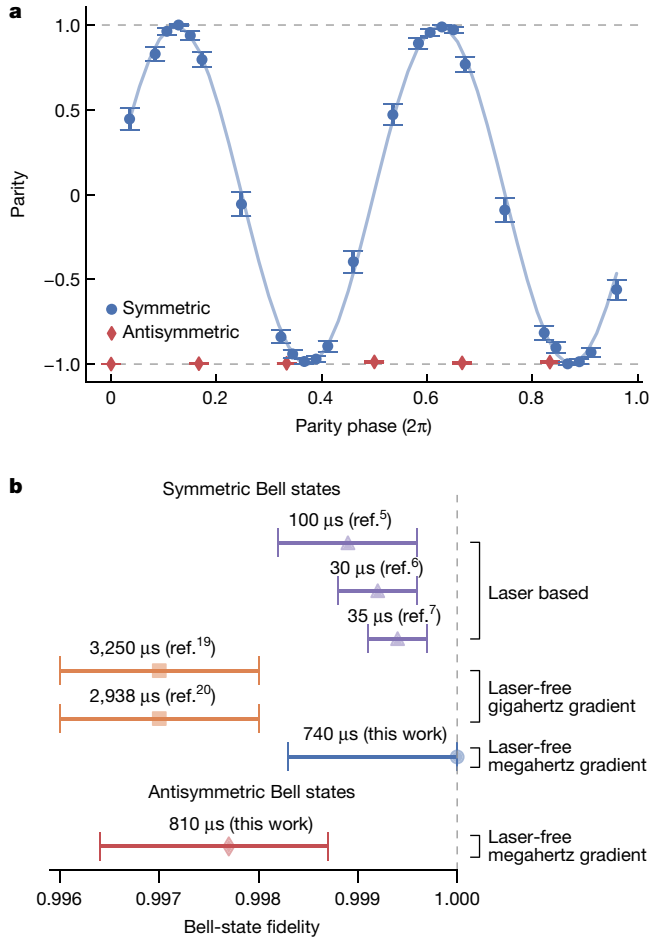

Fig. 3 | Entangled-state fidelity analysis. a, Parity of symmetric and antisymmetric Bell states. After creating the Bell state, we apply a global π/2 analysis pulse with a variable phase, and then measure the resulting state's parity ($P_0 + P_2 - P_1$). The symmetric Bell state $|\Phi\rangle = \frac{1}{\sqrt{2}}(|\downarrow\downarrow\rangle + i|\uparrow\uparrow\rangle)$ (blue circles) exhibits a sinusoidal parity oscillation (blue line shows best fit). We also create the antisymmetric state $|\Psi_-\rangle = \frac{1}{\sqrt{2}}(|\downarrow\uparrow\rangle - |\uparrow\downarrow\rangle)$ using individual ion addressing. This state has a constant parity close to −1 (red diamonds), as it is invariant under global rotations. Error bars indicate 68% confidence intervals. **b**, Comparison of the highest-fidelity Bell states created in trapped ion qubits with laser-based and laser-free techniques. We plot corrected Bell-state fidelities, as described in the respective references (ref. [7] has no correction), and 68% confidence intervals, and list the durations of the entangling operations. Results from the literature with lower Bell-state fidelities than those presented here are not shown.

we observe a constant parity as a function of the analysis pulse phase, as shown in Fig. 3a. We use the same 'trigger' technique as before to choose the reported dataset, which has a $|\Psi_-\rangle$ Bell-state fidelity of 0.9977, again corrected for the initialization error on $|\downarrow\downarrow\rangle$; to the best of our knowledge, this is the highest reported fidelity in any platform for such an antisymmetric Bell state. Bootstrapping yields a 68% confidence interval for the Bell-state fidelity of [0.9964, 0.9987], with a median bootstrap (Supplementary Information) fidelity of 0.9976. We do not correct for any error in the individual addressing operation in this fidelity estimate. Imperfect calibration of the required duration and phase of the individual addressing operation, an effect that could be mitigated by use of a composite pulse sequence, may account for the reduced fidelity compared with our symmetric entangled state.

Our results highlight the potential of laser-free techniques for universal control of trapped ion qubits for quantum computing and simulation. This technology offers potential advantages for scaling of trapped-ion quantum processors by enabling entangling operations to be carried out simultaneously in multiple trapping zones[50] in a multizone ion trap[16,51], as the control currents can produce the necessary gradients and fields in multiple zones at the same time. The entanglement of any particular group of ions could be enabled simply by adjusting the trap confinement in that zone with static potentials applied to local trapping electrodes, shifting the motional mode frequency of each zone in or out of resonance with the entangling interaction. The ability to perform many entangling operations simultaneously may reduce or eliminate the speed penalty relative to laser-based operations, which are often performed serially on different sets of ions due to laser power constraints. The tolerance of our laser-free method to drifts or offsets in driving parameters, as well as other sources of decoherence, relaxes the requirements for the fields to be exactly the same across all zones, and the scheme does not rely on carefully tuned trap electrode dimensions to achieve high fidelity[20,35]. Changes in the local trapping potentials can also be used to select which ions are temporarily frequency-shifted for individual qubit control. Entanglement between qubits in different ion species could be achieved by adding another pair of weak microwave tones for each different qubit frequency; any magnetic-field-sensitive Zeeman or hyperfine qubit transition can be used. These features may enable a new large-scale, multizone ion-trap quantum computing architecture using a two-ion-species qubit/helper design, where all qubit operations aside from ion loading are carried out with radiofrequency or microwave signals, along with microwatt-scale laser beams for the helper species. These laser beams could be delivered efficiently to all zones using integrated optics[21,22]. With the addition of trap-integrated photon detectors for qubit readout[23,24] and trap-integrated circuitry to generate confining potentials[52], it may be possible to realize a large-scale, fully integrated, high-fidelity trapped-ion quantum processor with no need for free-space optical access and dramatically reduced electrical interconnect requirements. Laser-free mixed-species entanglement may also be useful for molecular[53] or highly charged ions[54], or trapped electrons[55] or positrons, where suitable optical transitions for quantum logic operations may not be readily available.

Online content

Any methods, additional references, Nature Research reporting summaries, source data, extended data, supplementary information, acknowledgements, peer review information; details of author contributions and competing interests; and statements of data and code availability are available at https://doi.org/10.1038/s41586-021-03809-4.

1. Barenco, A. et al. Elementary gates for quantum computation. *Phys. Rev. A* **52**, 3457–3467 (1995).
2. Jozsa, R. in *The Geometric Universe: Science, Geometry, and the work of Roger Penrose* (eds Huggett, S. A, Mason, L. J., Tod, K. P., Tsou, S. T. & Woodhouse, N. M. J.) 369 (Oxford Univ. Press, 1998).
3. Georgescu, I. M., Ashhab, S. & Nori, F. Quantum simulation. *Rev. Mod. Phys.* **86**, 153–185 (2014).
4. Kimble, H. J. The quantum internet. *Nature* **453**, 1023–1030 (2008).
5. Ballance, C. J., Harty, T. P., Linke, N. M., Sepiol, M. A. & Lucas, D. M. High-fidelity quantum logic gates using trapped-ion hyperfine qubits. *Phys. Rev. Lett.* **117**, 060504 (2016).
6. Gaebler, J. P. et al. High-fidelity universal gate set for $^{9}Be^{+}$ ion qubits. *Phys. Rev. Lett.* **117**, 060505 (2016).
7. Clark, C. R. et al. High-fidelity Bell-state preparation with $^{40}Ca^{+}$ optical qubits. Preprint at https://arxiv.org/abs/2105.05828 (2021).
8. Harty, T. P. et al. High-fidelity preparation, gates, memory, and readout of a trapped-ion quantum bit. *Phys. Rev. Lett.* **113**, 220501 (2014).
9. Schmidt-Kaler, F. et al. Realization of the Cirac–Zoller controlled-NOT quantum gate. *Nature* **422**, 408–411 (2003).
10. Debnath, S. et al. Demonstration of a small programmable quantum computer with atomic qubits. *Nature* **536**, 63–66 (2016).
11. Wright, K. et al. Benchmarking an 11-qubit quantum computer. *Nat. Commun.* **10**, 5464 (2019).
12. Erhard, A. et al. Characterizing large-scale quantum computers via cycle benchmarking. *Nat. Commun.* **10**, 5347 (2019).
13. Barrett, M. D. et al. Deterministic quantum teleportation of atomic qubits. *Nature* **429**, 737–739 (2004).
14. Ruster, T. et al. Entanglement-based dc magnetometry with separated ions. *Phys. Rev. X* **7**, 031050 (2017).

15. Pino, J. M. et al. Demonstration of the trapped-ion quantum CCD computer architecture. *Nature* **592**, 209–213 (2021).
16. Wineland, D. J. et al. Experimental issues in coherent quantum-state manipulation of trapped atomic ions. *J. Res. Natl Inst. Stand. Technol.* **103**, 259–328 (1998).
17. Mintert, F. & Wunderlich, C. Ion-trap quantum logic using long-wavelength radiation. *Phys. Rev. Lett.* **87**, 257904 (2001).
18. Ospelkaus, C. et al. Trapped-ion quantum logic gates based on oscillating magnetic fields. *Phys. Rev. Lett.* **101**, 090502 (2008).
19. Harty, T. P. et al. High-fidelity trapped-ion quantum logic using near-field microwaves. *Phys. Rev. Lett.* **117**, 140501 (2016).
20. Zarantonello, G. et al. Robust and resource-efficient microwave near-field entangling $^{9}Be^{+}$ gate. *Phys. Rev. Lett.* **123**, 260503 (2019).
21. Mehta, K. K. et al. Integrated optical multi-ion quantum logic. *Nature* **586**, 533–537 (2020).
22. Niffenegger, R. J. et al. Integrated multi-wavelength control of an ion qubit. *Nature* **586**, 538–542 (2020).
23. Todaro, S. L. et al. State readout of a trapped ion qubit using a trap-integrated superconducting photon detector. *Phys. Rev. Lett.* **126**, 010501 (2021).
24. Setzer, W. et al. Fluorescence detection of a trapped ion with a monolithically integrated single-photon-counting avalanche diode. Preprint at https://arxiv.org/abs/2105.01235 (2021).
25. Cirac, J. I. & Zoller, P. Quantum computations with cold trapped ions. *Phys. Rev. Lett.* **74**, 4091 (1995).
26. Milburn, G. J., Schneider, S. & James, D. F. V. Ion trap quantum computing with warm ions. *Fortschr. Phys.* **48**, 801–810 (2000).
27. Sørensen, A. & Mølmer, K. Quantum computation with ions in thermal motion. *Phys. Rev. Lett.* **82**, 1971–1974 (1999).
28. Sørensen, A. & Mølmer, K. Entanglement and quantum computation with ions in thermal motion. *Phys. Rev. A* **62**, 022311 (2000).
29. Leibfried, D., Blatt, R., Monroe, C. & Wineland, D. Quantum dynamics of single trapped ions. *Rev. Mod. Phys.* **75**, 281–324 (2003).
30. Nägerl, H. C. et al. Laser addressing of individual ions in a linear ion trap. *Phys. Rev. A* **60**, 145 (1999).
31. Monroe, C., Meekhof, D. M., King, B. E., Itano, W. M. & Wineland, D. J. Demonstration of a fundamental quantum logic gate. *Phys. Rev. Lett.* **75**, 4714–4717 (1995).
32. Leibfried, D. et al. Experimental demonstration of a robust, high-fidelity geometric two ion-qubit phase gate. *Nature* **422**, 412–415 (2003).
33. Ozeri, R. et al. Errors in trapped-ion quantum gates due to spontaneous photon scattering. *Phys. Rev. A* **75**, 042329 (2007).
34. Ospelkaus, C. et al. Microwave quantum logic gates for trapped ions. *Nature* **476**, 181–184 (2011).
35. Hahn, H. et al. Integrated $^{9}Be^{+}$ multi-qubit gate device for the ion-trap quantum computer. *npj Quantum Inf.* **5**, 70 (2019).
36. Khromova, A. et al. Designer spin pseudomolecule implemented with trapped ions in a magnetic gradient. *Phys. Rev. Lett.* **108**, 220502 (2012).
37. Weidt, S. et al. Trapped-ion quantum logic with global radiation fields. *Phys. Rev. Lett.* **117**, 220501 (2016).
38. Leibfried, D. Individual addressing and state readout of trapped ions utilizing rf micromotion. *Phys. Rev. A* **60**, R3335 (1999).
39. Johanning, M. et al. Individual addressing of trapped ions and coupling of motional and spin states using rf radiation. *Phys. Rev. Lett.* **102**, 073004 (2009).
40. Warring, U. et al. Individual-ion addressing with microwave field gradients. *Phys. Rev. Lett.* **110**, 173002 (2013).
41. Sutherland, R. T. et al. Versatile laser-free trapped-ion entangling gates. *New J. Phys.* **21**, 033033 (2019).
42. Hayes, D. et al. Coherent error suppression in multiqubit entangling gates. *Phys. Rev. Lett.* **109**, 020503 (2012).
43. Srinivas, R. et al. Trapped-ion spin-motion coupling with microwaves and a near-motional oscillating magnetic field gradient. *Phys. Rev. Lett.* **122**, 163201 (2019).
44. Sackett, C. A. et al. Experimental entanglement of four particles. *Nature* **404**, 256–259 (2000).
45. Sutherland, R. T. et al. Laser-free trapped-ion entangling gates with simultaneous insensitivity to qubit and motional decoherence. *Phys. Rev. A* **101**, 042334 (2020).
46. Emerson, J., Alicki, R. & Życzkowski, K. Scalable noise estimation with random unitary operators. *J. Opt. B* **7**, S347–S352 (2005).
47. Knill, E. et al. Randomized benchmarking of quantum gates. *Phys. Rev. A* **77**, 012307 (2008).
48. Piltz, C., Sriarunothai, T., Varón, A. F. & Wunderlich, C. A trapped-ion-based quantum byte with 10^{-5} next-neighbour cross-talk. *Nat. Commun.* **5**, 4679 (2014).
49. Aude Craik, D. P. L. et al. High-fidelity spatial and polarization addressing of $^{43}Ca^{+}$ qubits using near-field microwave control. *Phys. Rev. A* **95**, 022337 (2017).
50. Leibfried, D., Knill, E., Ospelkaus, C. & Wineland, D. J. Transport quantum logic gates for trapped ions. *Phys. Rev. A* **76**, 032324 (2007).
51. Kielpinski, D., Monroe, C. & Wineland, D. J. Architecture for a large-scale ion-trap quantum computer. *Nature* **417**, 709 (2002).
52. Stuart, J. et al. Chip-integrated voltage sources for control of trapped ions. *Phys. Rev. Appl.* **11**, 024010 (2019).
53. Chou, C.-W. et al. Preparation and coherent manipulation of pure quantum states of a single molecular ion. *Nature* **545**, 164–165 (2017).
54. Kozlov, M. G., Safronova, M. S., Crespo López-Urrutia, J. R. & Schmidt, P. O. Highly charged ions: optical clocks and applications in fundamental physics. *Rev. Mod. Phys.* **90**, 045005 (2018).
55. Matthiesen, C., Yu, Q., Guo, J., Alonso, A. M. & Häffner, H. Trapping electrons in a room-temperature microwave Paul trap. *Phys. Rev. X* **11**, 011019 (2021).

Data availability

Source data are provided with this paper. All other data that support the plots within this paper and other findings of this study are available from the corresponding authors upon reasonable request.

Code availability

All simulation code or analysis code that support the plots within this paper and other findings of this study are available from the corresponding authors upon reasonable request.

Acknowledgements We thank C. J. Ballance, T. P. Harty, J. P. Gaebler, S. B. Libby, D. M. Lucas, V. M. Schäfer and T. R. Tan for helpful discussions. We thank M. Affolter and A. L. Collopy for insightful comments on the manuscript. At the time the work was performed, R.S., S.C.B., H.M.K., A.K., and D.T.C.A. were supported as associates in the Professional Research Experience Program (PREP) operated jointly by the National Institute of Standards and Technology (NIST) and the University of Colorado Boulder under award number 70NANB18H006 from the US Department of Commerce, NIST. This work was supported by the NIST Quantum Information Program and ONR.

Author contributions R.S. and H.M.K. carried out the experiments, assisted by S.C.B., D.T.C.A and D.H.S.; D.H.S., R.S., H.M.K., A.K. and R.T.S. analysed the data and performed numerical simulations, with support from E.K. and S.G.; D.T.C.A., D.H.S., R.S., S.C.B. and H.M.K. built and maintained the experimental apparatus; R.S. wrote the manuscript with input from all authors; A.C.W., D.L., D.H.S. and D.J.W. secured funding for the work; and D.H.S. and D.T.C.A. supervised the work with support from A.C.W., D.L., S.G., E.K. and D.J.W.

Competing interests The authors declare no competing interests.

Additional information

Supplementary information The online version contains supplementary material available at https://doi.org/10.1038/s41586-021-03809-4.

Correspondence and requests for materials should be addressed to R. Srinivas or D. H. Slichter.

Peer review information *Nature* thanks Tracy Northup, Christian Roos and the other, anonymous, reviewer(s) for their contribution to the peer review of this work. Peer reviewer reports are available.